

# Acceleration to high velocities and heating by impact using Nike KrF laser.

Max Karasik,<sup>1,\*</sup> J. L. Weaver,<sup>1</sup> Y. Aglitskiy,<sup>2</sup> T. Watari,<sup>3</sup> Y. Arikawa,<sup>3</sup> T. Sakaiya,<sup>3</sup> J. Oh,<sup>4</sup> A. L. Velikovich,<sup>1</sup> S. T. Zalesak,<sup>1</sup> J. W. Bates,<sup>1</sup> S. P. Obenschain,<sup>1</sup> A. J. Schmitt,<sup>1</sup> M. Murakami,<sup>3</sup> and H. Azechi<sup>3</sup>

<sup>1</sup>*Plasma Physics Division, Naval Research Laboratory, Washington DC 20375*

<sup>2</sup>*SAIC, McLean, VA 22102*

<sup>3</sup>*Institute of Laser Engineering, Osaka University, 2-6 Yamada-oka, Suita, Osaka 565-0871, Japan*

<sup>4</sup>*RSI, Lanham, MD 20706*

The Nike krypton fluoride laser [S. P. Obenschain, S. E. Bodner, D. Colombant, K. Gerber, R. H. Lehmberg, E. A. McLean, A. N. Mostovych, M. S. Pronko, C. J. Pawley, A. J. Schmitt, et al., *Phys. Plasmas* **3**, 2098 (1996)] is used to accelerate planar plastic foils to velocities that for the first time reach 1000 km/s. Collision of the highly accelerated deuterated polystyrene foil with a stationary target produces  $\sim 1$  Gbar shock pressures and results in heating of the foil to thermonuclear temperatures. The impact conditions are diagnosed using DD fusion neutron yield, with  $\sim 10^6$  neutrons produced during the collision. Time-of-flight neutron detectors are used to measure the ion temperature upon impact, which reaches 2 – 3 keV.

PACS numbers: 42.55.Lt, 42.60.-v, 42.60.Jf, 52.57.-z, 89.30.Jj

## I. INTRODUCTION

Here we discuss experiments that explore the acceleration of near solid density planar targets to extremely high speeds ( $\sim 1000$  km/sec) using a krypton fluoride laser. These velocities exceed those needed for even the highest velocity designs contemplated for inertial fusion implosions (400–500 km/s) [1]. Collisions of the high velocity targets provide a means to obtain pressures above 1 Gbar, a regime of interest to high energy density physics. The temperatures and pressures are high enough at 1000 km/s to produce thermonuclear neutrons when employing targets containing deuterium. The velocities reported here are to our knowledge the highest achieved by laser acceleration of material, and approach those thought to be needed for impact ignition [2].

Aside from using a specially designed, long (tens of km) linear accelerator [3], laser driven ablation appears to be the only method of accelerating bulk matter to such speeds. Speeds of 700 km/s have been achieved previously on a third harmonic Nd:glass ( $\lambda = 351$  nm) Gekko/HIPER laser at Osaka University [4]. There are several challenges to achieving speeds  $\sim 1000$  km/s. It requires coupling  $\sim 0.5$  GJ/g of kinetic energy to the target while keeping the target near solid density, or at the very least, above the critical density. The speeds required are close to or higher than the exhaust velocity, requiring most of the target mass to be ablated. Furthermore, given a limited laser energy the target is necessarily thin, making it more susceptible to heating due to radiation transport from the corona and to breakup due to the Rayleigh-Taylor instability (RTI). RTI effectively limits the distance over which the target can be accelerated before breaking apart. Achieving the highest previous velocities on a glass laser required the use of special

techniques to mitigate RTI, such as double ablation using high-Z dopants [4] and two-color irradiation [5]. A way to mitigate this situation is to keep the non-uniformities seeding the instability to a minimum and apply increased pressure to accelerate the target over a shorter distance, while making use of ablative stabilization to reduce the RTI growth rates [6].

Utilizing a short wavelength (248 nm) KrF laser makes the task significantly easier. Shorter wavelength results in ablation at higher densities, giving higher ablation pressure for a given intensity. It also allows higher intensity on target before the onset of deleterious laser-plasma instabilities [7]. Finally, the application of induced spatial incoherence (ISI) smoothing [8] gives an ultra-uniform illumination of the target, limiting the seeding of the RTI.

This paper is organized as follows. Sec. II describes the experimental setup, Sec. III gives the experimental results, Sec. IV discusses the results together with analytic modeling and simulations; finally, conclusions are drawn in Sec. V.

## II. EXPERIMENTAL SETUP

Fig. 1 shows the experimental setup. Targets consist of two foils: the first one 10–16  $\mu\text{m}$  thick polystyrene, the second 15–20  $\mu\text{m}$  thick graphite. The laser [8] with the pulsed shape and spatial profile shown in Fig. 2 irradiates the first foil, causing it to ablatively accelerate and impact the second foil. The distance between foils is varied between 500 and 700  $\mu\text{m}$ . Both foils are significantly wider than the laser spot size ( $\approx 2$  mm on the side vs. 0.46 mm FWHM, respectively). The trajectory of the flyer is obtained by imaging it side-on onto the slit of a streak camera using monochromatic x-ray imaging at 1.86 keV with a spherically bent quartz crystal [9]. The image is either from backlighting and self-emission, or self-emission only (no backlighter). The amount of self-

---

\*Electronic address: karasik@nrl.navy.mil

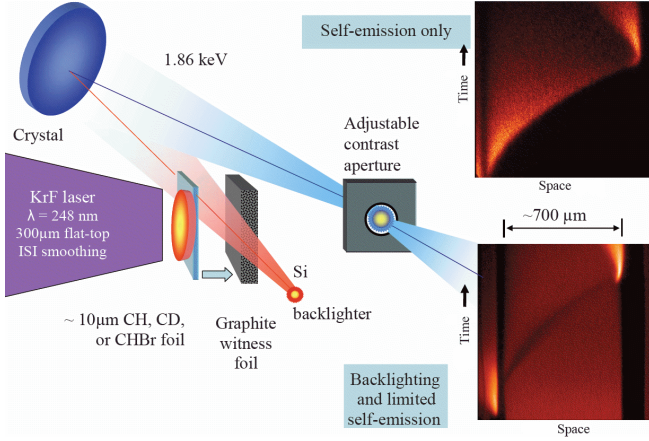


FIG. 1: (Color online) Schematic of the experimental setup. Shown is the laser-illuminated polystyrene foil followed by the graphite witness foil. Also shown schematically is the side-on imaging using Bragg reflection from a curved crystal. The adjustable contrast aperture placed in the image plane of the backlighter source controls the amount of self-emission x-rays reaching the detector. The lower inset on the right shows an image of a shot with backlighting and self-emission. The upper inset is a shot with self-emission only.

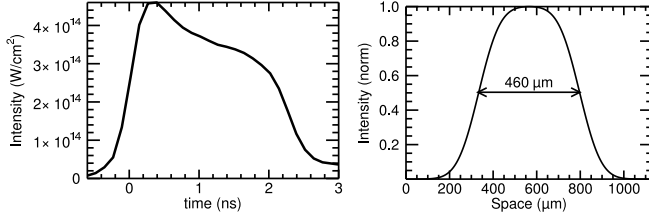


FIG. 2: Laser pulshape (left) and spatial profile lineout (right).  $t = 0$  corresponds to the half-rise of the laser intensity on target.

emission imaged is controlled by an aperture placed at the image plane of the backlighter source[9]. Backlighting is done using a Si target irradiated by dedicated laser beams. Timing of the streak camera with respect to the laser pulse is set using the time of half-rise of x-ray self-emission from the target front surface, with an estimated uncertainty of  $\pm 100$  ps.

The impact of the accelerated first foil generates a strong shock in both foils. Visible light emission from the shock breakout on the rear of the second foil is imaged onto a slit of a streak camera using an  $f/3$  optic. The polystyrene is pure CH, pure CD, or either of the two with 0.4% (atomic) Br doping. Five neutron time-of-flight (nTOF) detectors are positioned at various angles around the target: three at approx. 2.6 m from the target, and two at 3.6 m.

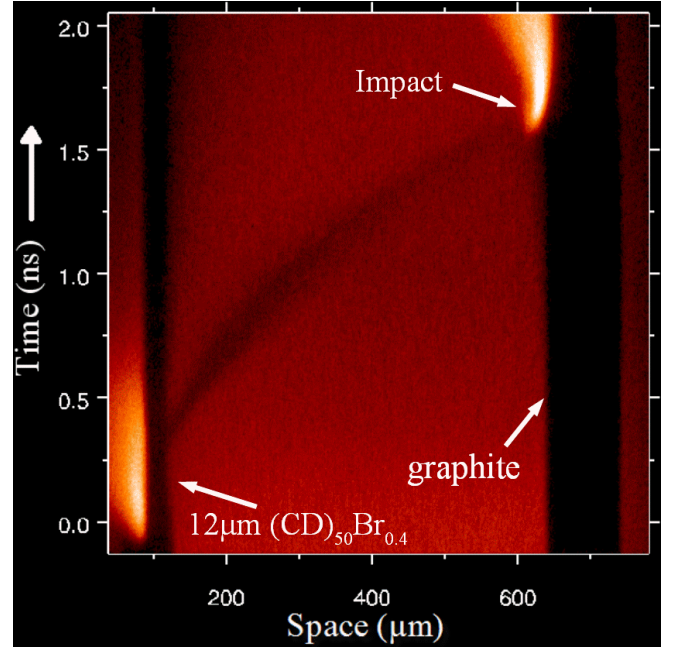


FIG. 3: Sample side-on streak camera image with backlighting and self-emission. The laser is shining from the left. Visible are shadows of the two foils with the accelerated part of the first foil in between. Strong x-ray self-emission is visible at the point of impact.

### III. EXPERIMENTAL RESULTS

#### A. Acceleration

A sample side-on streak camera image is shown in Fig. 3. X-rays from both backlighting and self-emission are imaged in this shot. The vertical shadows are of the first foil ( $12\mu\text{m}$  deuterated polystyrene doped with 0.4 at% of Br) and of the graphite second foil. The shadow of the accelerating part of the first foil is visible in between. Self-emission is visible initially from the first foil during the initial peaked part of the pulse. Strong self-emission appears at the point of impact with the second foil starting at about 1.6 ns.

Without the Br doping, the trajectory of the accelerated target is not so readily observable with backlighting, in particular because carbon opacity at 1.86 keV drops dramatically as temperature rises above 100 eV. Self-emission is a much higher contrast technique in this case. A sample image of self-emission only with the trajectory traced out is shown in Fig. 4. In this case the backlighting is turned off and the contrast aperture is fully open to allow all the self-emission at 1.86 keV reflected from the crystal to be imaged onto the streak camera. In this way the self-emission from the target is visible throughout the acceleration, and peaks strongly when the impact occurs.

The target trajectory can readily be traced in the im-

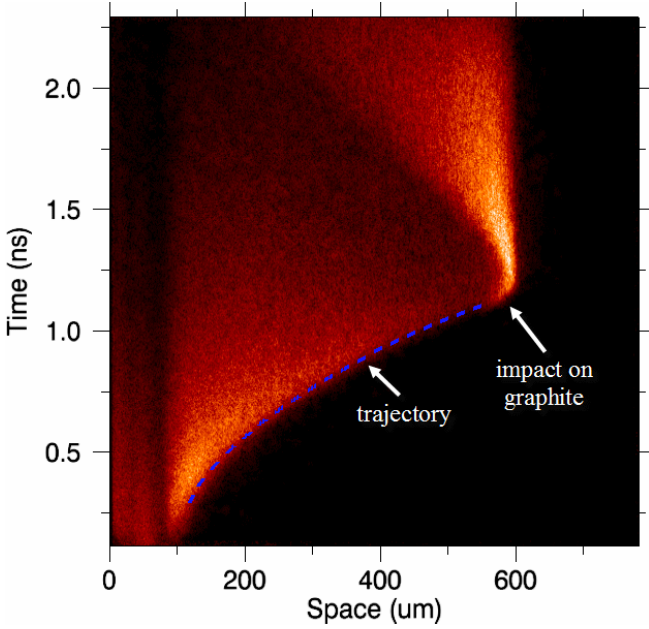


FIG. 4: Sample side-on image of the accelerating  $10.5 \mu\text{m}$  CH target taken with self-emission only. The trajectory traced from the image is overlaid as a dashed line. The impact on graphite marked by bright emission is clearly visible.

age as the boundary of self-emission (shown as dashed line overlaid on the image in Fig. 4). The trajectory is fitted with a polynomial and differentiated to obtain the target velocity. The velocity from the trajectory of Fig. 4 is shown in Fig. 5.

The procedure used to fit the trajectory and obtain the velocity is as follows. At each spatial pixel of the image, the time pixel of the half-rise of the self-emission is found. The resulting  $[t, x(t)]$  data points are least-squares fitted with a fourth-degree polynomial. Fourth degree polynomial was chosen for physics reasons as well as because it reduces the  $\chi^2$  error of the fit [10] as compared to a lower degree polynomial. A second degree polynomial would imply constant acceleration of the foil, whereas an increase in acceleration is expected as the mass is ablated. A third degree polynomial would give constant increase in acceleration, however variation in acceleration is expected to be non-linear due to the decrease in laser intensity in time as well as target mass reduction owing to ablation. Increasing the polynomial degree further results in higher uncertainty in the fit without a physical reason to do so.

The fourth degree polynomial obtained from the fit of the trajectory is then differentiated to obtain the velocity as a third degree polynomial. The error bars on velocity have been obtained by two independent methods. The first method assumes that the errors in the trajectory points are normally distributed and uses the matrix of covariances of the errors of fit coefficients of the trajectory and error propagation [11]. The second method uses

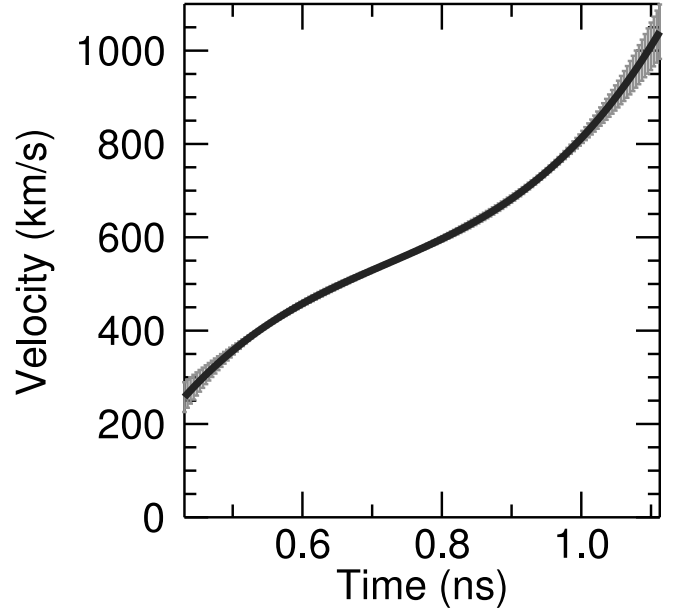


FIG. 5: Velocity of the  $10.5 \mu\text{m}$  CH target obtained from the side-on image in Fig 4. The acceleration increases toward the end as the target mass is ablated away. The error bars (one standard deviation) obtained from error analysis of the trajectory fit are shown in gray.

a Monte Carlo-like “bootstrap” method [10], where the error estimate is obtained by redoing the trajectory fit many times on data sets synthesized from the original data by replacing a random fraction of the points with others from the same data set. The two error estimates agreed to better than 20%. The larger of the two was used for the one standard deviation error bars shown in Fig 5.

The velocity trace shows the acceleration decreasing as the drive intensity drops (Fig. 2), then increasing again after  $t = 0.9$  ns as the drive intensity levels off and as a significant portion of the target mass is ablated away. The increasing acceleration toward the end is also prominent in the simulations, as will be seen in Section IV B. The target is moving at just over 1000 km/s prior to the impact.

Fig. 6 shows a streak image of the visible light emitted from the rear surface of the second foil for the same shot as Figs. 4 and 5. Shock breakout appears at  $t = 1.24 \pm 0.05$  ns. This is just after the collision seen on the side-on image at  $t = 1.20 \pm 0.05$  ns. For an impact pressure  $\sim 1$  Gbar, the shock speed in graphite is expected to be  $\sim 250 \mu\text{m/ns}$  [12]. For a  $15 \mu\text{m}$  thick graphite, this implies shock breakout approximately 60 ps after the collision (assuming a steady shock), in reasonable agreement with the observation. The width of the emission breakout is approximately  $200 \mu\text{m}$  FWHM at the time of the shock breakout and  $300 \mu\text{m}$  FWHM at the time of the peak emission (110 ps later), indicating that the width of the flyer is comparable to the flat-top of the laser profile,

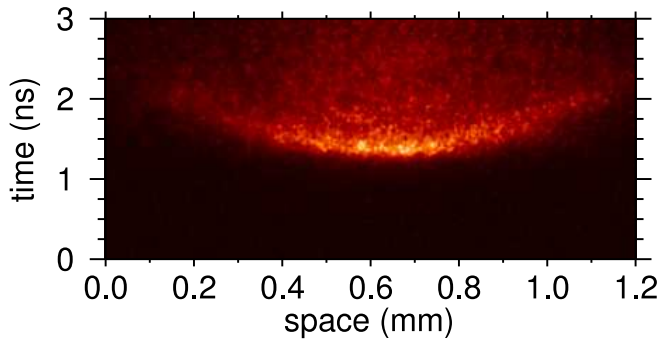


FIG. 6: (Color online) Streaked image of visible light emission from the rear surface of the second foil. Shock breakout occurs at  $t = 1.24$  ns, consistent with the impact time from the side-on imaging. The spatial extent of the initial breakout is consistent with the width of the laser flat-top.

as expected. Significantly the shock breakout is continuous spatially, indicating that the target integrity was maintained up to the collision.

Shots with significantly thinner foils ( $\leq 10 \mu\text{m}$ ) allowed to accelerate over longer distances ( $\approx 800 \mu\text{m}$ ) show clear signs of going underdense, such as trajectory breakup concurrent with the appearance of self-emission from the laser shining through to the second foil.

### B. Diagnosing the impact via neutron production

If the accelerated foil is deuterated, a readily measurable neutron yield is observed on impact. Five neutron detectors spaced at various angles around the target chamber were utilized. Two of the detectors were absolutely calibrated at the Gekko XII facility in Osaka University; the other three were cross-calibrated to them. A sample neutron signal and fit are shown in Fig. 7 for a  $12 \mu\text{m}$  CD foil initially  $700 \mu\text{m}$  from the graphite. No significant anisotropy in neutron yield was found, supporting the expectation that the neutrons are thermonuclear. The arrival time of the neutrons is as expected for 2.45 MeV DD neutron energy. The yield on this shot was measured to be  $(1.3 \pm 0.3) \times 10^6$  neutrons. For an accelerated CD foil when the second foil is not present, on the other hand (no impact takes place), the yield is measured to be only  $\sim 5 \times 10^4$  neutrons – much smaller, as expected, with DD reactions taking place only in the laser illuminated low density corona.

Ion temperature is inferred from the time-of-flight spread in the neutron signal [13] such as in Fig. 7 as follows. The neutron signal is fitted by a convolution of the detector response with the Gaussian spread in the neutron arrival times due to the ion temperature. The detector response is a convolution of an exponential decay of the scintillator, a square pulse due to finite thickness of the scintillator, and the impulse response of the photomultiplier/cable/oscilloscope system. The fitting

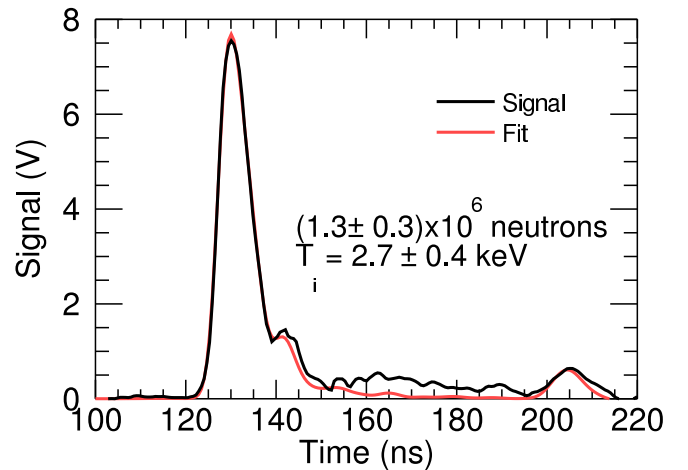


FIG. 7: (Color online) Neutron signal (black) and convolution fit (red) for a  $12 \mu\text{m}$  thick CD foil.  $t = 0$ , as before, corresponds to the half-rise of the laser intensity on target; the detector-target distance is  $2.70$  m; given that the impact occurred at  $t = 2$  ns, the  $2.45$  MeV neutrons are expected to arrive at  $t = 127$  ns, consistent with the time of the rise of the signal.

function thus has the parameters of the Gaussian (width, amplitude, and peak location) and the decay time of the scintillator. The integral of the Gaussian is proportional to the neutron yield, the peak location gives the mean neutron arrival time, and the FWHM is related to the ion temperature:  $T_i \propto (\text{FWHM})^2$  [14]. The error bar on the temperature is estimated using analysis of Ref. 15.

An interesting result was seen when a higher density material (gold) was used in place of graphite second foil in some of the shots. The neutron yield did not increase as would be expected at first, but rather was an order of magnitude lower than that with the graphite second foil. A likely explanation is that a thin surface layer of the gold is pre-expanded by x-rays from the laser corona and cushions the impact, absorbing a significant fraction of the flyer kinetic energy. This is evident in the side-on backlighting, as seen in Fig. 8. Gold from the second foil is clearly expanding toward the first foil during the target acceleration, much more so than the graphite (Fig. 3). The difference is likely due to the high  $Z$  of Au, which would cause it to absorb the x-rays in a significantly thinner layer than graphite.

## IV. DISCUSSION

### A. Collision hydrodynamics

Useful information about the state of the flyer just before impact and the conditions reached upon impact can be obtained from the measured neutron yield and ion temperature. In order to interpret these results analytically, the hydrodynamics of the collision need to be ex-



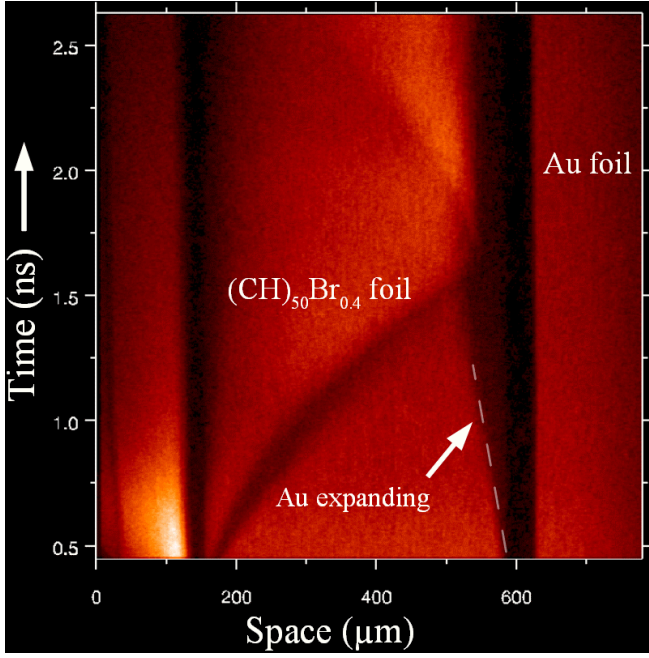


FIG. 8: Significant pre-expansion is observed when gold is used instead of graphite as the second foil. Dashed line marks the front edge of material expanding from the second foil.

amined.

For a CD flyer impacting a rigid wall, neglecting radiation and conduction losses, the kinetic energy of the flyer would be fully converted (less ionization energy) into thermal, heating the flyer to a temperature given by [16]:

$$T = 5.38 \left( \frac{V_0}{10^3 \text{ km/s}} \right)^2 - 0.077 \text{ keV}, \quad (1)$$

where  $V_0$  is the flyer velocity just prior to the impact.

When the second foil is not a rigid wall but is compressible, some of the kinetic energy of the flyer is imparted to the second foil, generating a moving interface between the two and driving a shock into both. This is illustrated in Fig. 9, which shows an analytic 1D hydrodynamics  $x$ - $t$  diagram of density and temperature for a CD foil collision with a compressible wall (in this example Cu). In this case, Eq. 1 remains valid in the reference frame of the contact interface of the foils. The temperature obtained in the collision is reduced in that  $V_0$  in the above is substituted by an effective velocity  $V_{\text{eff}} = V_0 - V_{\text{interface}}$ .

Back-of-the-envelope estimates of accelerated foil density and unablated mass can be obtained as follows. Temperature  $T$  and neutron yield  $Y_n$  are obtained from nTOF detectors and  $V_0$  from side-on trajectory.  $V_{\text{eff}}$  can be obtained from  $T$  by solving:

$$T = 5.38 \left( \frac{V_{\text{eff}}}{10^3 \text{ km/s}} \right)^2 - 0.077 \text{ keV}, \quad (2)$$

The interface velocity  $V_{\text{interface}}$  is then obtained from  $V_{\text{interface}} = V_0 - V_{\text{eff}}$ . Equation of state (EOS) of the

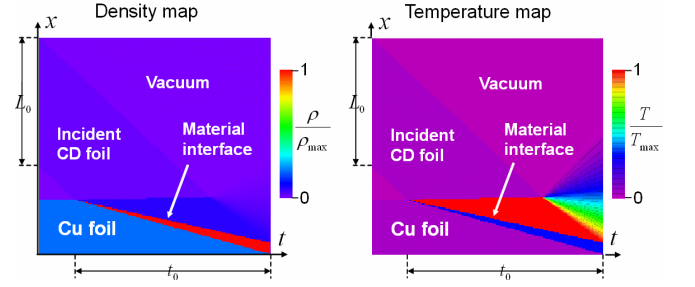


FIG. 9: Analytic hydrodynamics  $x$ - $t$  diagram of density (left) and temperature (right) for a CD foil collision with a compressible wall (in this case a Cu foil).  $\rho_{CD} = 0.8 \text{ g/cm}^3$  and  $v = 500 \text{ km/s}$ . Pressure at impact is 1.55 Gbar, shock speed in Cu is 148 km/s, Cu compression ratio is 4.9, and the interface velocity is 118 km/s, reducing the effective CD velocity at impact to 382 km/s.

second foil can be used to infer the collision pressure  $P$  knowing the interface velocity. The flyer density prior to the collision  $\rho_0$  can then be solved for from the expression for  $P$  obtained assuming ideal gas EOS for the flyer:

$$P = \frac{4}{3} \rho_0 V_{\text{eff}}^2 \quad (3)$$

The unablated CD areal mass can be computed from the neutron reactivity  $\langle \sigma v \rangle_{DD}$  (depends on  $T$  only) and the neutron yield  $Y_n$  by solving for the deuterium areal number density  $N_D$ :

$$Y_n = \frac{3}{8} \langle \sigma v \rangle_{DD} \frac{A N_D^2}{V_{\text{eff}}}, \quad (4)$$

where  $A$  is the area of the flyer.

This back-of-the-envelope estimate is applied to measurements from a particular shot in the table shown in Fig. 10. Because of a significant error bar on the measured temperature ( $2.7 \pm 0.4 \text{ keV}$ ), the inferred quantities in the table are calculated for the lower, middle, and upper values of temperature based on this error bar. In addition, for a particular temperature, the inferred unablated mass has an uncertainty due to the error bar on the neutron yield, while the inferred collision pressure and flyer density have an uncertainty due to the error bar on the flyer speed. These uncertainties are estimated by error propagation. As can be seen in the table, the temperature uncertainty has the dominant effect on the inferred values. To within a factor of 2 however, the inferred collision pressure is  $\sim 1 \text{ Gbar}$ , inferred flyer density prior to impact is  $\sim 1/10 \times$  solid, and approximately  $1 \mu\text{m}$  equivalent of solid CD remained unablated.

The simple analytic estimates above neglect a lot of physics that can be addressed in a comprehensive simulation of the collision, such as realistic density profiles for the flyer and the second foil, thermal conduction and radiation, and differences in ion and electron temperatures. For example, a recent analysis of such planar collisions by Gus'kov et al. [17] indicates that there may be

| Measured quantities |                                       |                          | Inferred quantities          |  |                                 |                            |   |
|---------------------|---------------------------------------|--------------------------|------------------------------|--|---------------------------------|----------------------------|---|
| T<br>(keV)          | Neutron<br>Yield<br>( $\times 10^5$ ) | Flyer<br>speed<br>(km/s) | Effective<br>speed<br>(km/s) | DD neutron<br>reactivity<br>( $\text{cm}^2/\text{s}$ ) | Collision<br>pressure<br>(Gbar) | Density of<br>flyer (g/cc) | Unablated CD<br>( $\mu\text{m}$ solid CD) |
| 2.3                 | $1.3 \pm 0.3$                         | $910 \pm 30$             | 665                          | $4.8\text{E-}21$                                       | $1.54 \pm 0.38$                 | $0.26 \pm 0.06$            | $1.39 \pm 0.16$                           |
| 2.7                 | $1.3 \pm 0.3$                         | $910 \pm 30$             | 718                          | $9.4\text{E-}21$                                       | $0.94 \pm 0.30$                 | $0.14 \pm 0.04$            | $1.03 \pm 0.12$                           |
| 3.1                 | $1.3 \pm 0.3$                         | $910 \pm 30$             | 768                          | $1.6\text{E-}20$                                       | $0.52 \pm 0.22$                 | $0.07 \pm 0.03$            | $0.81 \pm 0.09$                           |

FIG. 10: “Back-of-the-envelope” estimates of flyer density and remaining mass based on measured temperature, neutron yield and target velocity.

insufficient time for electron and ion temperature equilibration. If this were the case it would imply that a lower  $V_{\text{eff}}$  corresponds to the measured ion temperature. The inferred unablated mass is only weakly affected by this however, which can be seen as follows. Generalizing Eq. 2 for  $T_e \neq T_i$  and neglecting the ionization loss (0.077 keV) we get:

$$V_{\text{eff}} = \sqrt{\frac{3(kT_i + \bar{Z}kT_e)}{\bar{M}m_n}}, \quad (5)$$

where  $\bar{Z} = 3.5$  is the mean charge and  $\bar{M} = 7$  the mean atomic weight of CD and  $m_n$  is the atomic mass unit. From Eq. 4, for a given ion temperature and neutron yield,  $N_D \propto \sqrt{V_{\text{eff}}} \propto (T_i + \bar{Z}T_e)^{\frac{1}{4}}$ . Thus, for example, if  $T_e = 1/2 T_i$ ,  $N_D$  would only be reduced by 12%. Lower  $V_{\text{eff}}$  would likely imply however, that the second foil is pre-expanded, cushioning the impact. Future experiments will aim to measure  $T_e$  spectroscopically using a high-Z dopant in the flyer.

## B. Simulations

A significant benefit of the experiments like those discussed here is that they provide a useful platform for exercising and benchmarking radiation hydrodynamics codes. Some initial results of simulations of the flyer acceleration are presented in this section. Comprehensive simulations of the collision will be the subject of a separate article.

An important experimental result is that the target acceleration was sufficiently robust against the Raleigh-Taylor instability to maintain its integrity over a distance  $\sim 60\times$  its thickness. This result can be examined first by applying analytic RTI linear growth formula to a simple 1D simulation of the acceleration. Fig. 11 shows the time-integrated amplification of linear perturbations computed by post-processing a 1D simulation of a 12  $\mu\text{m}$  CD foil driven by the pulse in Fig. 2. The amplification is computed by integrating the growth rate given by the modified Takabe formula [18]. As can be seen in the figure, the maximum amplification factor is only about  $100\times$ . Given the ISI laser smoothing and a smooth foil (foils used in the experiment had 0.4 nm rms roughness), this implies perturbation growth to significantly less than 1  $\mu\text{m}$  amplitude – insufficient to break up the foil.

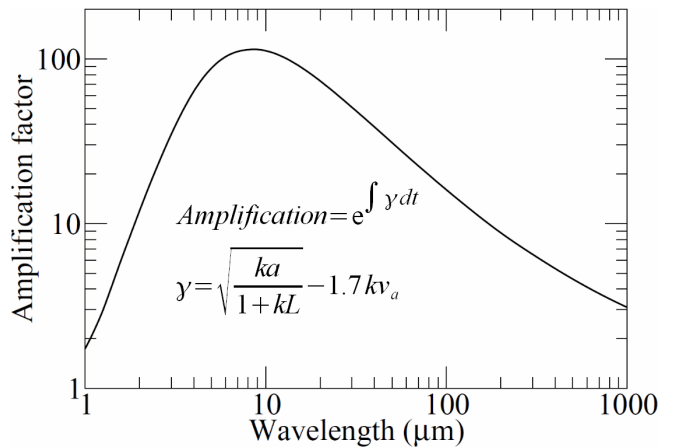


FIG. 11: Time-integrated amplification of linear perturbations (post-processing of 1D simulation). The parameters of the modified Takabe formula shown are taken from the simulation.

In order to examine stability as well as the effects of a finite spot size, a high resolution 2D axisymmetric simulation using NRL’s FASTRAD3D radiation hydrocode has been performed. Fig. 12 shows a plot of mass density from the simulation at a point in time when the target has traveled just over 550  $\mu\text{m}$  and reached 1000 km/s. The target is a 12  $\mu\text{m}$  CD foil driven by the pulseshape and spatial profile used in the experiment (Fig. 2); the simulation mesh size is 0.1  $\mu\text{m}$  along the laser axis and 3.5  $\mu\text{m}$  perpendicular to it. Although the finite-spot-size effect is prominent, the target has maintained its integrity. The peak density is 0.12 g/cm<sup>3</sup>, not far from the estimates obtained in Sec. IV A above. The “flat-top” portion of the target is 200–300  $\mu\text{m}$ , consistent with the shock breakout measurements (Fig. 6).

In order to examine the target trajectory, on-axis values of peak density, velocity, and distance traveled are taken from the 2D simulation above and are shown in Fig. 13. As can be seen in the figure, peak density decays after the initial shocks, but stabilizes during the later portion of the trajectory. The acceleration increases toward the end, similar to what is seen in the experiment (Fig. 5).

For a more direct comparison with the shot shown in Fig. 4, figure 14 shows the on-axis lineouts of a 2D axisymmetric simulation of a 10.5  $\mu\text{m}$  CH target. In addition to the trajectory and velocity of the peak of mass density, the plot shows the trajectory and the velocity of the edge of the x-ray emission in the 1.25–2.5 keV band. This x-ray energy band is centered on the 1.86 keV x-ray energy imaged in the experiment (Fig. 4). Both trajectories overlap to within the line thickness, while the velocities differ significantly only above 1100 km/s, where the density is dropping precipitously. Increase in acceleration prior to that is similar to that seen in the experiment (Fig. 5).

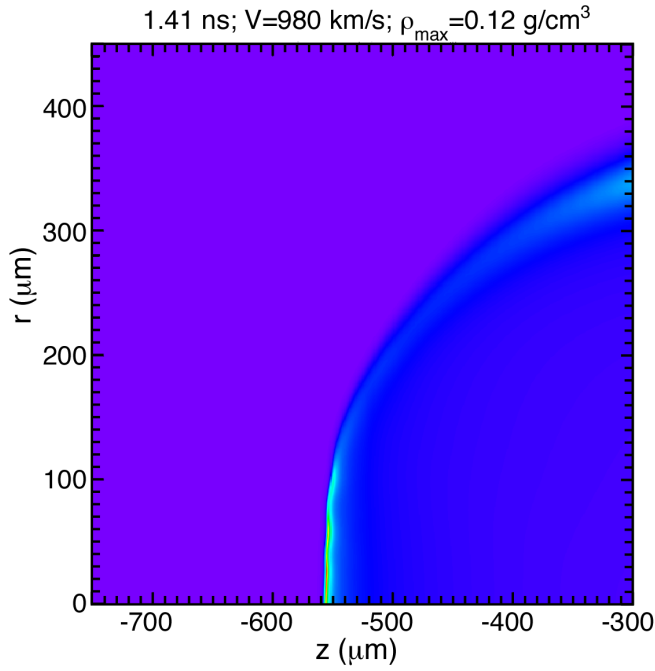


FIG. 12: (Color online) Mass density from an axisymmetric 2D simulation of a  $12\ \mu\text{m}$  CD foil after the target has traveled about  $550\ \mu\text{m}$ . The  $z$ -axis at the bottom of the figure is the axis of symmetry with the laser shining from the right; the simulation mesh size is  $0.1\ \mu\text{m}$  along the laser axis and  $3.5\ \mu\text{m}$  perpendicular to it. Peak density is  $0.12\ \text{g}/\text{cm}^3$ , velocity is  $980\ \text{km}/\text{s}$ , and “flat-top” portion of the target is  $200\text{--}300\ \mu\text{m}$ .

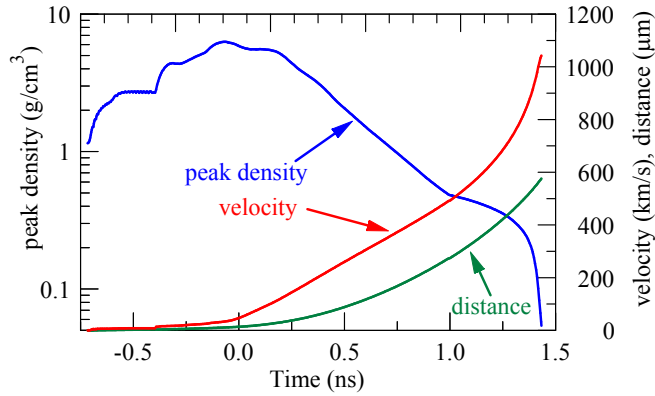


FIG. 13: (Color online) Peak density, target velocity, and distance traveled on the axis of the 2D simulation of Fig. 12 of a  $12\ \mu\text{m}$  CD foil.

## V. CONCLUSIONS

Target velocities on the order of  $1000\ \text{km}/\text{s}$  have been routinely achieved for the first time, opening up new op-

portunities. Utilizing a KrF laser allowed us to achieve this with as little as  $1\ \text{kJ}$  of energy. Higher velocities should be possible: higher laser energy would allow use of thicker targets that should reach higher velocities still.

Impact of the highly accelerated targets results in  $\sim\text{Gbar}$  pressures and heating to thermonuclear temperatures. Neutron production gives an effective diagnostic of the state upon impact. However, higher densities of the accelerated foils are needed for impact ignition. Future experiments will attempt to obtain these velocities with less preheat, which would allow higher in-flight densities.

## Acknowledgments

The authors would like to thank the Nike laser and target crews: R. Dicht, L. Granger, B. Jenkins, S. Kraf-sig, N. Nocerino, J. Picciotta, and S. Terrell. Support of T. J. Kessler and D. P. Brown was invaluable in fielding the targets and setting up the neutron detectors. Thanks to Schafer Laboratories for supplying the targets. This work was supported by the U.S. DOE and the Office of Naval Research.

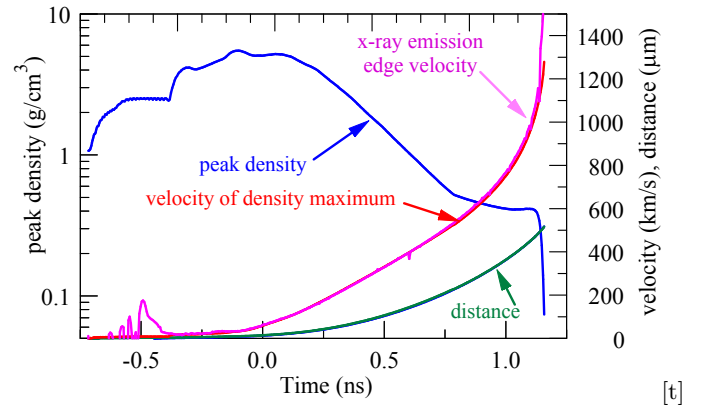


FIG. 14: (Color online) Peak density, target velocity, and distance traveled on the axis of a 2D axisymmetric simulation of a  $10.5\ \mu\text{m}$  CH foil. Increase in acceleration at the end is similar to that seen in the experiment (Fig. 5). In addition to the trajectory and velocity of the density maximum, the trajectory and velocity of the edge of the x-ray emission in the  $1.25\text{--}2.5\ \text{keV}$  band are plotted. Both trajectories overlap to within the line thickness (labelled “distance”), while the velocities differ significantly only above  $1100\ \text{km}/\text{s}$ .

- 
- [1] S. Obenschain, J. Sethian, and A. Schmitt, *Fusion Sci. and Technol.* **56**, 594 (2009).
  - [2] M. Murakami, H. Nagatomo, H. Azechi, F. Ogando, M. Perlado, and S. Eliezer, *Nucl. Fusion* **46**, 99 (2006).
  - [3] S. Olariu, *Nucl. Instr. and Meth. in Phys. Res. A* **366**, 376 (1995).
  - [4] H. Azechi, T. Sakaiya, T. Watari, M. Karasik, H. Saito, K. Ohtani, K. Takeda, H. Hosoda, H. Shiraga, M. Nakai, et al., *Phys. Rev. Lett.* **102**, 235002 (2009).
  - [5] K. Otani, K. Shigemori, T. Sakaiya, S. Fujioka, A. Sunahara, M. Nakai, H. Shiraga, H. Azechi, and K. Mima, *Phys. Plasmas* **14**, 122702 (2007).
  - [6] S. E. Bodner, D. G. Colombant, J. H. Gardner, R. H. Lehmberg, S. P. Obenschain, L. Phillips, A. J. Schmitt, J. D. Sethian, R. L. McCrory, Q. Seka, et al., *Phys. Plasmas* **5**, 1901 (1998).
  - [7] J. L. Weaver, J. Oh, L. S. Phillips, J. F. Seely, U. Feldman, D. M. Kehne, B. B. Afeyan, et al., *Observations of the two plasmon decay instability driven by the Nike KrF laser*, To be submitted to *Phys. Rev. Lett.*
  - [8] S. P. Obenschain, S. E. Bodner, D. Colombant, K. Gerber, R. H. Lehmberg, E. A. McLean, A. N. Mostovych, M. S. Pronko, C. J. Pawley, A. J. Schmitt, et al., *Phys. Plasmas* **3**, 2098 (1996).
  - [9] Y. Aglitskiy, T. Lehecka, S. Obenschain, S. Bodner, C. Pawley, K. Gerber, J. Sethian, C. M. Brown, J. Seely, U. Feldman, et al., *Appl. Optics* **37**, 5253 (1998).
  - [10] W. H. Press, S. A. Teukolsky, W. T. Vetterling, and B. P. Flannery, *Numerical Recipes in FORTRAN; The Art of Scientific Computing* (Cambridge University Press, New York, 1993).
  - [11] P. R. Bevington and D. K. Robinson, *Data Reduction and Error Analysis for the Physical Sciences* (McGraw-Hill, New York, 1992).
  - [12] P. R. Levashov, V. E. Fortov, K. V. Khishchenko, I. N. Lomov, and I. V. Lomonosov, in *Shock Compression of Condensed Matter 1997*, edited by Schmidt, Dandekar, and Forbes (The American Institute of Physics, Melville, New York, 1998), pp. 47–50, shock wave database available at <http://teos.ficp.ac.ru/rusbank/>.
  - [13] H. Brysk, *Plasma Physics* **15**, 611 (1973).
  - [14] T. J. Murphy, R. E. Chrien, and K. A. Klare, *Rev. Sci. Instrum.* **68**, 610 (1997).
  - [15] R. A. Lerche and B. A. Remington, *Rev. Sci. Instrum.* **61**, 3131 (1990).
  - [16] A. L. Velikovich and M. Murakami, *J. Plasma Fusion Res.* **83**, 831 (2007).
  - [17] S. Y. Gus'kov, H. Azechi, N. N. Demchenko, I. Y. Doskoch, M. Murakami, V. B. Rozanov, T. Sakaiya, T. Watari, and N. V. Zmitrenko, *Plasma Phys. Contr. F.* **51**, 095001 (2009).
  - [18] S. Atzeni and J. Meyer-ter-Vehn, *The Physics of Inertial Fusion* (Clarendon Press, Oxford, 2004), p. 268.